From General to Specific: Online Updating for Blind Super-Resolution

Shang Li[a,b], Guixuan Zhang[a], Zhengxiong Luo[a,b],
Jie Liu[a,*], Zhi Zeng[a], Shuwu Zhang[a,b]

[a]*Institute of Automation, Chinese Academy of Sciences*
[b]*School of Artificial Intelligence, University of Chinese Academy of Sciences*
No.95, Zhongguancun East Road, Beijing 100190, PR China

Abstract

Most deep learning-based super-resolution (SR) methods are not image-specific: 1) They are trained on samples synthesized by predefined degradations (*e.g.* bicubic downsampling), regardless of the domain gap between training and testing data. 2) During testing, they super-resolve all images by the same set of model weights, ignoring the degradation variety. As a result, most previous methods may suffer a performance drop when the degradations of test images are unknown and various (*i.e.* the case of blind SR). To address these issues, we propose an online SR (ONSR) method. It does not rely on predefined degradations and allows the model weights to be updated according to the degradation of the test image. Specifically, ONSR consists of two branches, namely internal branch (IB) and external branch (EB). IB could learn the specific degradation of the given test LR image, and EB could learn to super resolve images degraded by the learned degradation. In this way, ONSR could customize a specific model for each test image, and thus get more robust to various degradations. Extensive experiments on both synthesized and real-world images show that ONSR can generate more visually favorable SR results and achieve state-of-the-art performance in blind SR.

Keywords: blind super-resolution, online updating, internal learning, external learning

*Corresponding author
Email addresses:* lishang2018@ia.ac.cn (Shang Li), guixuan.zhang@ia.ac.cn
(Guixuan Zhang), luozhengxiong2018@ia.ac.cn (Zhengxiong Luo), jie.liu@ia.ac.cn (
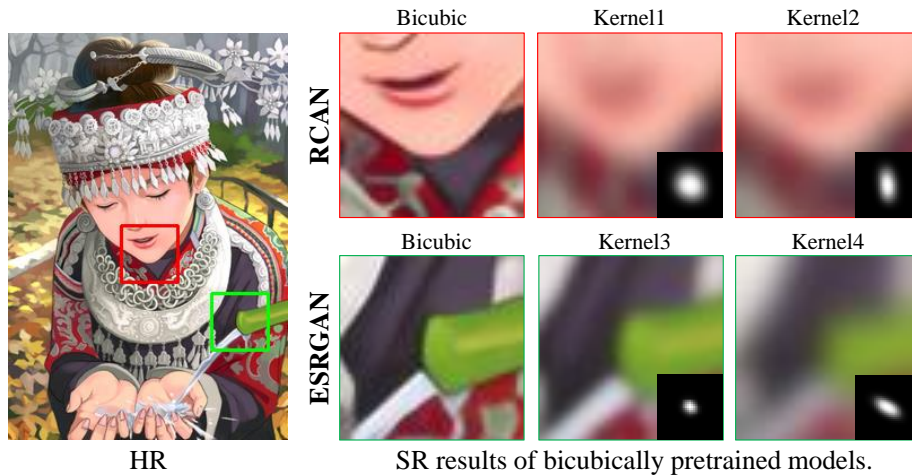Jie Liu), zhi.zeng@ia.ac.cn (Zhi Zeng), shuwu.zhang@ia.ac.cn (Shuwu Zhang)

Figure 1: The adaptation problem of the offline trained ESRGAN and RCAN. The corresponding blur kernel is at the bottom right of each image.

1. Introduction

Single image super-resolution (SISR) aims to reconstruct a plausible high-resolution (HR) image from its low-resolution (LR) counterpart. As a fundamental vision task, it has been widely applied in video enhancement, medical imaging and surveillance imaging. Mathematically, the HR image $\mathbf{x}$ and LR image $\mathbf{y}$ are related by a degradation model

$$\mathbf{y} = (\mathbf{k} \otimes \mathbf{x}) \downarrow_s +\mathbf{n}, \tag{1}$$

where $\otimes$ represents two-dimensional convolution of $\mathbf{x}$ with blur kernel $\mathbf{k}$, $\downarrow_s$ denotes the s-fold downsampler, and $\mathbf{n}$ is usually assumed to be additive, white Gaussian noise (AWGN) [1]. The goal of SISR is to restore the corresponding HR image of the given LR image, which is a classical ill-posed inverse problem.

Recently, super-resolution (SR) has been continuously advanced by various deep learning-based methods. Although these methods have exhibited promising performance, there is a common limitation: they are too 'general' and not image-specific. Firstly, they are exhaustively trained via LR-HR image pairs synthesized by predefined degradations, ignoring the real degradations of test images (*i.e.* non-blind SR). For example, most no-blind SR methods are optimized by paired samples synthesized with

2

Bicubic degradation [2, 3, 4]. And many blind SR methods also use Gaussian blur kernels to synthesize data to optimize their SR modules, such as IKC [5] and DASR [6]. When the degradations of test images are different from the predefined ones, they may suffer a significant performance drop. Secondly, their model weights are fixed during testing, and all images are super-resolved by the same set of weights. However, test images are usually degraded by a wide range of degradations. If the model performs well for certain degradations, it is likely to perform badly for others. Thus, super-resolving all images with the same model weights may lead to sub-optimal results. For example, as shown in Figure 1, ESRGAN [3], and RCAN [2] are trained via bicubically synthesized LR-HR pairs. They have excellent performance on bicubically downscaled images but may produce undesirable results when the images are blurred by unseen kernels.

Towards these issues, we propose an online updating network namely ONSR, which 1) synthesizes the training data according to the degradation of the test image, instead of by predefined degradations, and 2) updates the SR model weights for each test image instead of keeping the model fixed. Specifically, we design two branches, namely internal branch (IB) and external branch (EB). For each given test image, IB tries to learn the internal degradation via adversarial training [7]. With the learned degradation, EB degrades HR images from external datasets to LR-HR pairs, which are then used to update the SR module. Since the degradation is adaptively learned, the domain gap between synthesized training data and the test image could be bridged. And as the SR module can be updated for each test image, it may also get more robust to test images with a large degradation variety.

In summary, our main contributions are as follows:

- Towards the unknown and various degradations in blind SR, we propose an online SR method. It could customize a specific model for each test LR image and thus could have more robust performance in different cases.

- We design two learning branches, IB and EB. They could learn the degradation of the given test image and adaptively update the SR module according to learned degradation.

3

- Extensive experiments on both synthesized and real-world images show that ONSR can generate more visually favorable SR results and achieve state-of-the-art performance on blind SR.

2. Related Works

As shown in Table 1, nowadays SR methods can be roughly divided into two categories: non-blind and blind. Blind SR methods assume that the degradation of the test image is predefined (such as bicubic downsampling) or has been estimated by degradation-prediction methods. While blind SR methods do not need extra information about the degradation.

Table 1: Examples of non-blind and blind SR methods. Non-blind SR methods assume that the degradation of the test image is predefined or has been estimated by other methods. While blind SR methods assume that the degradation is unavailable.

Non-blind SR methods	Blind SR methods
SRCNN [8], RCAN [2], RRDB [3]	Ji *et al*. [11], Cornillere *et al*. [12], dSRVAE [13]
ZSSR [9], SRMD [10], USRNet [1]	KernelGAN+ZSSR [14], IKC [1], DASR [6]

2.1. Non-Blind Super-Resolution

In non-blind SR the degradation is predefined or known beforehand, which is easier to be studied. Thus most early SR methods are non-blind. These methods are usually trained with paired LR-HR samples synthesized by predefined degradation [15], such as bicubic downsampling. Since Dong *et al*. propose the first convolution neural network for SR (SRCNN) of bicubically downscaled images and achieves remarkable performance. In the following years, researchers focus on developing various network architectures. For example, the residual dense network (RDN) [16] proposed by Zhang *et al*. and the residual-in-residual dense block (RRDB) [3] proposed by Wang *et al*. apply skip connections [17] and dense connections [18] to make the SR network deeper and hierarchical features more discriminative. The residual channel attention network

(RCAN) [2] proposed by Zhang *et al.*, the channel attention and spatial graph convolutional network (CASG) [4] proposed by Yang *et al.*, and the multi-attention augmented network (MAAN) [19] proposed by Chen *et al.* all use attention mechanism to further enhance the representation capability. Although these methods have largely advanced the SR performance for bicubic downsampling, they usually perform poorly for other degradations. To alleviate this problem, Zhang *et al.* propose two networks namely SRMD [10] and USRNet [1]. They input the test image and its degradation simultaneously into the network, in which way, the SR network can handle test images with various degradations. However, these methods require extra accurate degradation-estimation methods which are also left to be studied. Thus, in this paper, the proposed method focuses on blind SR, which does not need degradation prediction and is more applicable.

2.2. Blind Super-Resolution

Blind SR is much more challenging, as it is difficult for a single model to generalize to different degradations. In [20], the final results are ensembled from models that are capable of handling different cases. The SR modules in IKC [5], DASR [6] and that proposed by Cornillere [12] are all pretrained by synthesized data pairs containing a variety of degradations to be more robust to different degradations. But there are countless degradations, and we cannot train a model for each of them. Other methods try to utilize the internal prior of the test image itself. In [21], the model is finetuned via similar pairs searched from the test image. Irani *et al.* propose [22] and KernelGAN [14] where the blur kernel is firstly estimated by maximizing the similarity of recurring patches across multi-scale of the LR image, and then used to synthesize LR-HR training samples. Ji *et al.* [11] also use a similar idea as KernelGAN to estimate degradations. However, the number of internal patches is limited, which heavily restricts the performance of these methods. Different from these completely internal learning-based methods, our ONSR can apply the degradation information via internal learning to external HR data, which helps to better optimize the SR module. In this way, ONSR can simultaneously take the benefits of internal and external priors in the LR and HR images respectively.
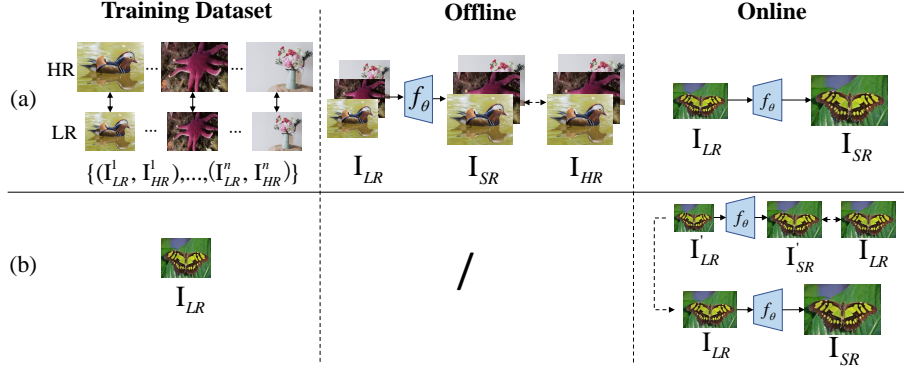
Figure 2: (a) Offline training scheme. Training datasets are synthesized from external HR image. The SR model are trained offline and only perform inference online. (b) The online training scheme of ZSSR [9]. Only the test image is used as the training data. The SR model is trained online.

2.3. Offline & Online Training in Super-Resolution

Most deep learning-based SR methods are offline optimized, *i.e.* their model weights are only updated during training via the LR-HR pairs synthesized from external data, while keep fixed during testing. Thus, the learned model weights are completely determined by external data, without considering the inherent information of the test image. Consequently, LR images degraded by various degradations may get super-resolved by the same set of model weights. It is likely that the model only performs well on certain types of images while failing on others. Contrary to offline training, online training can get the test LR image involved in model optimization. For example, ZSSR [9] is an online trained SR method. It is optimized by the test LR image and its downscaled version. Therefore, it can customize the network weights for each test LR image, and could have more robust performance over different images. However, the training samples of most online trained models are limited to only one test image [22, 9, 14]. It will heavily restrict their performance. Instead, in addition to the test LR image, our ONSR can also utilize the external HR images during the online training phase. And in this way, it could better incorporate general priors of the external data and the inherent information of the test LR image.

6

3. Method

3.1. Motivation

As we have discussed above, previous non-blind SR methods are usually offline trained (as shown in Figure 2(a)) [15], which means LR images with various degradations are super-resolved with the same set of weights, regardless of the specific degradation of the test image. Towards this problem, a straightforward idea is to adopt an online training algorithm, *i.e.* adjust the model weights for each test LR image with different degradations. A similar idea namely "zero-shot" learning is used in ZSSR. As shown in Figure 2(b), ZSSR is trained with the test LR image and its downscaled version. However, this pipeline has two in-born drawbacks: 1) with a limited number of training samples, it only allows relatively simple network architectures to avoid overfitting, thus adversely affecting the representation capability of deep learning. 2) No HR images are involved. It is difficult for the model to learn general priors of HR images, which is also essential for SR reconstruction [23].

The drawbacks of ZSSR motivate us to think: a better online updating algorithm should be able to utilize both the test LR image and external HR images. The former provides inherent information about the degradation method, and the latter enables the model to exploit better general priors. Therefore, a "general" SR model can be adjusted to process the test LR image according to its "specific" degradation, which we call: from "general" to "specific".

3.2. Formulation

Accoring to the framework of MAP (maximum a posterior) [24], the blind SR can be formulated as:

$$(\mathbf{k}, \mathbf{x}) = \underset{\mathbf{k}, \mathbf{x}}{\arg\max} \|\mathbf{y} - (\mathbf{k} \otimes \mathbf{x}) \downarrow_s \|^2 + \mu\phi(\mathbf{x}) + \nu\varphi(\mathbf{k}) \tag{2}$$

where $\|\mathbf{y} - (\mathbf{k} \otimes \mathbf{x}) \downarrow_s \|^2$ is the fidelity term. $\phi(\mathbf{x})$ and $\varphi(\mathbf{k})$ model the priors of sharp image and blur kernel. μ and ν are trade-off regularization parameters. Although many delicate handcrafted priors, such as the sparsity of the dark channel [25], L_0-regularized intensity [26], and the recurrence of the internal patch [27], have been
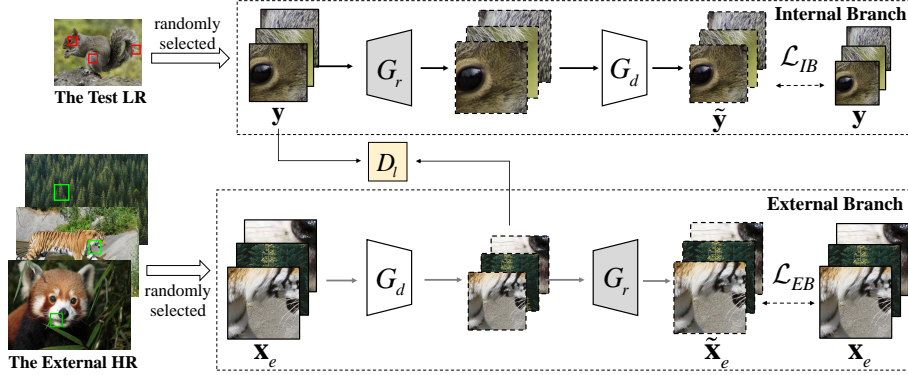
7

Figure 3: The online updating scheme of ONSR. Top: internal branch. Bottom: external branch. Images with solid borders are the input. Images with dotted borders are the output of G_r or G_d.

suggested for $\phi(\mathbf{x})$ and $\varphi(\mathbf{k})$, these heuristic priors could not cover more concrete and essential characteristics of different LR images. To circumvent this issue, we design two modules, *i.e.* the reconstruction module G_r and the degradation estimation module G_d, which can capture priors of $\mathbf{x}$ and $\mathbf{k}$ in a learnable manner. We substitute $\mathbf{x}$ by $G_r(\mathbf{y})$, and denote the degradation process as $G_d(\cdot)$, then the problem becomes:

$$\arg\min_{\theta_{G_r},\theta_{G_d}} \|\mathbf{y} - G_d(G_r(\mathbf{y};\theta_{G_r});\theta_{G_d})\|, \tag{3}$$

The prior terms are removed because they could also be captured by the generative networks $G_r(\cdot)$ and $G_d(\cdot)$ [23].

This problem involves the optimization of two neural networks, *i.e.* G_r and G_d. Thus, we can adopt an alternating optimization strategy:

$$\begin{cases} \theta_{G_r}^{i+1} = \arg\min_{\theta_{G_r}} \|\mathbf{y} - G_d(G_r(\mathbf{y};\theta_{G_r});\theta_{G_d}^i)\| \\ \theta_{G_d}^{i+1} = \arg\min_{\theta_{G_d}} \|\mathbf{y} - G_d(G_r(\mathbf{y};\theta_{G_r}^i);\theta_{G_d})\|. \end{cases} \tag{4}$$

In the first step, we fix G_d and optimize G_r, while in the second step we fix G_r and optimize G_d.

So far only the given LR image is involved in this optimization. However, as we have discussed in Sec 3.1, the limited training sample may be not enough to get G_r sufficiently optimized, because there are usually too many learnable parameters in G_r.

Thus, we introduce the external HR images $\mathbf{x}_e$ in the optimization of G_r. In the ith step, we degrade the $\mathbf{x}_e$ by $G_d(\,\cdot\,;\theta^i_{G_d})$ to $\mathbf{y}_e$. Then $\mathbf{x}_e$ and $\mathbf{y}_e$ could form a paired sample that could be used to optimize G_r. Thus, the alternating optimization process becomes:

$$
\begin{cases}
\mathbf{y}_e = G_d(\mathbf{x}_e; \theta^i_{G_d}) \\
\theta^{i+1}_{G_r} = \underset{\theta_{G_r}}{\arg\min} \, \|\mathbf{x}_e - G_r(\mathbf{y}_e; \theta_{G_r})\| \\
\theta^{i+1}_{G_d} = \underset{\theta_{G_d}}{\arg\min} \, \|\mathbf{y} - G_d(G_r(\mathbf{y}; \theta^i_{G_r}); \theta_{G_d})\|,
\end{cases}
\tag{5}
$$

in which, G_r is optimized by external datasets, while G_d is optimized by the given LR image only. At this point, we have derived the proposed method from the perspective of alternating optimization. This may help better understand OSNR.

3.3. Online Super-Resolution

As illustrated in Figure 3, our online SR (ONSR) consists of two branches, *i.e.* IB and EB. IB and EB share the reconstruction module G_r and the degradation estimation module G_d. G_r aims to map the given LR image $\mathbf{y}$ from the LR domain $\mathcal{Y} \subset \mathbb{R}^{3 \times H \times W}$ to the HR domain $\mathcal{X} \subset \mathbb{R}^{3 \times sH \times sW}$, *i.e.* reconstructing an SR image $\mathbf{x}$. While G_d aims to estimate the specific degradation of the test LR image.

In IB, only the given LR image is involved. As shown in Figure 3, the input of IB are patches randomly selected from the test LR image. The input LR patch $\mathbf{y} \sim p_{\mathcal{Y}}$ is firstly super resolved by G_r to an SR patch. Then this SR patch is further degraded by G_d to a fake LR patch. To guarantee that the fake LR can be translated to the original LR domain, It is supervised by the original LR patch via L1 loss. The paired SR and LR patches could help G_d to learn the specific degradation of the test image. The optimization details will be further explained in Section 3.4.

In EB, only external HR images are involved. The input of EB are patches randomly selected from different external HR images. Conversely, the external patch $\mathbf{x}_e \sim p_{\mathcal{X}}$ is firstly degraded by G_d to a fake LR patch, . As the weights of G_d are shared between IB and EB, the external patches are actually degraded by the learned degradation. Thus, the paired HR and fake LR patches could help G_r learn to super resolve LR images with specific degradations.

According to the above analysis, the loss functions of IB and EB can be formulated as:

$$\mathcal{L}_{IB} = \mathbb{E}_{\mathbf{y} \sim p_{\mathcal{Y}}} \|\mathbf{y} - G_d(G_r(\mathbf{y}; \theta_{G_r}); \theta_{G_d})\|_1, \tag{6}$$

$$\mathcal{L}_{EB} = \mathbb{E}_{\mathbf{x}_e \sim p_{\mathcal{X}}} \|\mathbf{x}_e - G_r(G_d(\mathbf{x}_e; \theta_{G_d}); \theta_{G_r})\|_1. \tag{7}$$

Since information in the single test LR image is limited, to help G_d better learn the specific degradation, we further adopt the adversarial learning strategy. As shown in Figure 3, we introduce a discriminator D_l. D_l is used to discriminate the distribution characteristics of the LR image. It could force G_d to generate fake LR patches that are more similar to the real ones. Thus more accurate degradations could be learned by G_d. We use the GAN formulation as follows,

$$\mathcal{L}_{GAN} = \mathbb{E}_{\mathbf{y} \sim p_{\mathcal{Y}}}[log D_l(\mathbf{y}; \theta_{D_l})] + \mathbb{E}_{\mathbf{x}_e \sim p_X}[log(1 - D_l(G_d(\mathbf{x}_e; \theta_{G_d}); \theta_{D_l}))]. \tag{8}$$

Adversarial training is not used for the intermediate output $G_r(\mathbf{y})$, because it may lead $G_r(\mathbf{y})$ to generate unrealistic textures [3].We also experimentally explain this problem in Section 4.4.3.

3.4. Separate Optimization

Generally, most SR networks are optimized by the weighted sum of all objectives. All modules in an SR network are treated indiscriminately. Unlike this commonly used joint optimization method, we propose a separate optimization strategy. Specifically, G_d is optimized by the objectives that are directly related to the test LR image, while G_r is optimized by objectives that are related to external HR images. The losses for these two modules are as follows,

$$\mathcal{L}_{G_d} = \mathcal{L}_{IB} + \lambda \mathcal{L}_{GAN} \tag{9}$$

$$\mathcal{L}_{G_r} = \mathcal{L}_{EB} \tag{10}$$

where λ controls the relative importance of the two losses.

Algorithm 1 Algorithm of ONSR

Input: The LR image to be reconstructed: I_{LR}

  The external HR image dataset: $\boldsymbol{S}_{HR}$

  Maximum updating step: T

  Online testing step interval: t

Output: The best SR image: $\boldsymbol{I}_{SR} = G_r(I_{LR};\ g_r)$

  1: Load the pretrained model G_r

  2: $i = 0$

  3: **while** $i \leq T$ **do**

  4:      $i \leftarrow i + 1$

  5:      Sample n LR image patches $\{\mathbf{y}^j\}_{j=1}^n$ from I_{LR}

  6:      Sample n HR image patches $\{\mathbf{x}_e^j\}_{j=1}^n$ from $\boldsymbol{S}_{HR}$

  7:      *// Online testing*

  8:      **if** $i\%t == 0$ **then**

  9:          $I_{SR}^i = G_r^i(I_{LR};\ g_r^i)$

  10:     **end if**

  11:     *// Online updating different modules*

  12:     Update $\theta_{G_d} \leftarrow \theta_{G_d} - (\nabla_{\theta_{G_d}}\mathcal{L}_{IB} + \lambda\nabla_{\theta_{G_d}}\mathcal{L}_{GAN})$

  13:     Update $\theta_{G_r} \leftarrow \theta_{G_r} - \nabla_{\theta_{G_r}}\mathcal{L}_{EB}$

  14:     Update $\Delta\theta_{D_l} \leftarrow \theta_{D_l} - \lambda\nabla_{\theta_{D_l}}\mathcal{L}_{GAN}$

  15: **end while**

We adopt this separate optimization strategy for two reasons. Firstly, as the analysis in Section 3.2 that G_d and G_r are alternately optimized in ONSR, separate optimization may make these modules easier to converge [1]. Secondly, G_d aims to learn the specific degradation of the test image, while G_r needs to learn the general priors from external HR images. Thus it is more targeted for them to be separately optimized. We experimentally prove the superiority of separate optimization in Sec 4.4.4. The overall algorithm is shown in Algorithm 1.
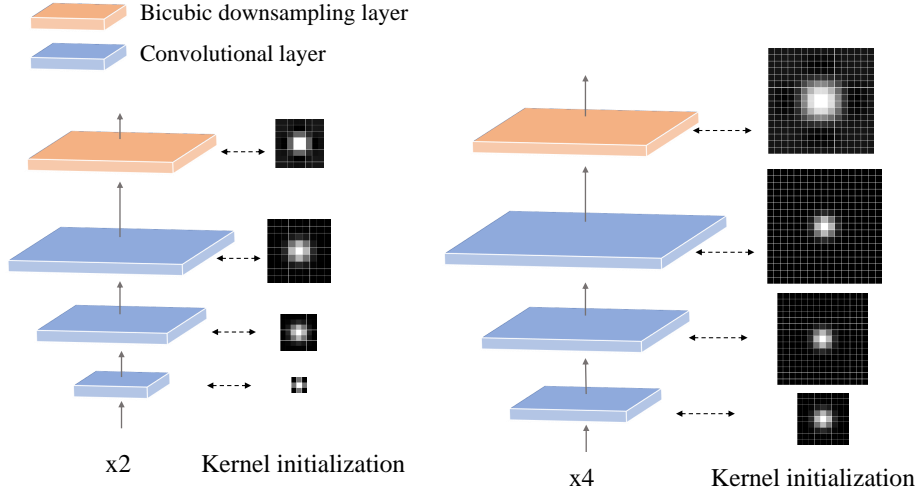
Figure 4: The architecture and initialization of G_d.

3.5. Network Instantiation

Most existing SR structures can be used as G_r and integrated into ONSR. In this paper, we mainly use Residual-in-Residual Dense Block (RRDB) [3]. RRDB combines the multi-level residual network and dense connections, which is easy to be trained and has promising performance on SR. G_r consists of 23 RRDBs and an upsampling module. It is initialized using the pre-trained network parameters, which could render additional priors of external data, and also provide a comparatively reasonable initial point to accelerate optimization.

The architecture of the degradation module G_d is shown in Figure 4. We can see that blurring and downsampling are linear transforms in Eq. 1, so G_d is designed as a deep linear network. Theoretically, a single convolutional layer should be able to represent all possible downsampling blur methods in Eq. 1. However, linear networks have infinitely many equal global minimums according to [28], which makes the gradient-based optimization faster for deeper linear networks than shallower ones. Thus, we employ three convolutional layers with no activations and a bicubic downsampling layer in G_d. The bicubic downsampling layer could help obtain a reasonable initial point, which is similar to that in [14] but simpler. Additionally, to accelerate the convergence of G_d, we use isotropic Gaussian kernels with a standard deviation of 1 to

12

initialize all convolutional layers, as shown in Figure 4. Considering that images with larger downsampling factor are usually more seriously degraded, we set the size of the three convolutional layers to 3×3, 7×7, 9×9 for scale factor $\times 2$, and 9×9, 15×15, 17×17 for scale factor $\times 4$.

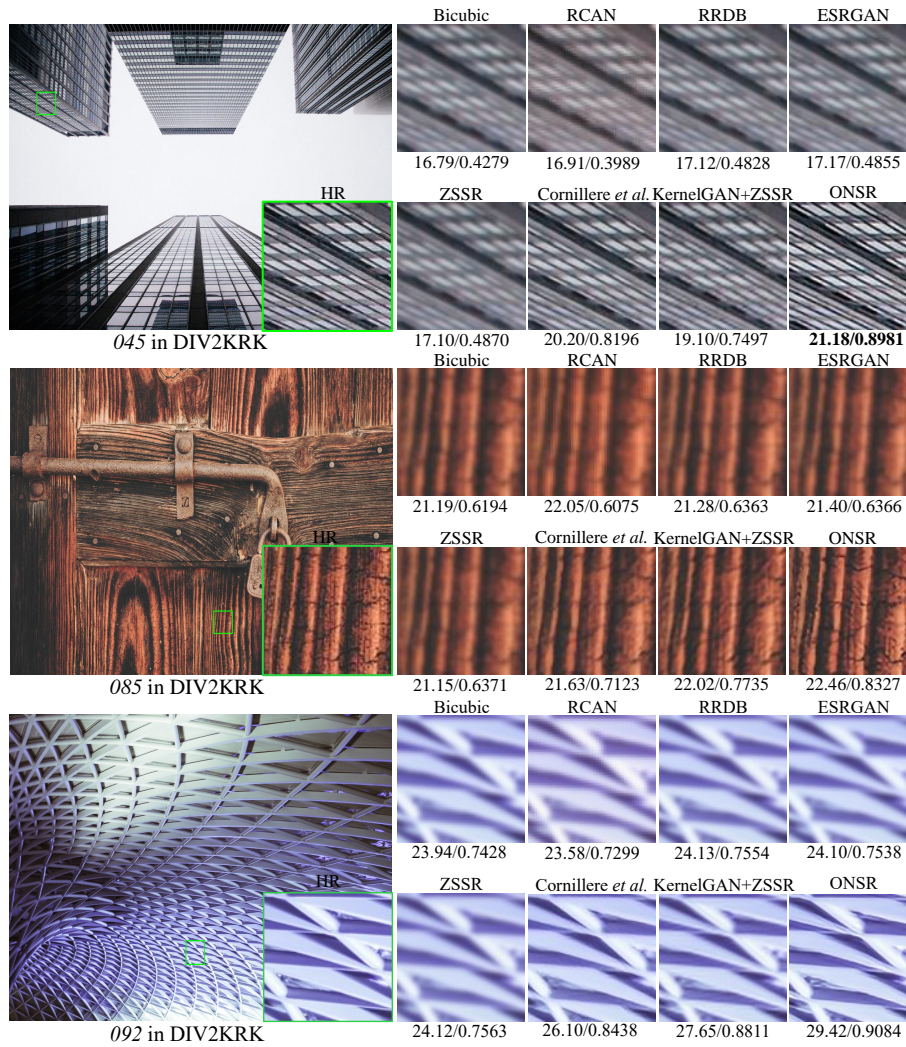D_l is a VGG-style network [29] to perform discrimination. The input size of D_l is 32×32.

Figure 5: Visual comparison of ONSR and SotA SR methods for $2\times$ SR. The model name is denoted above the corresponding patch and PSNR/SSIM is denoted below.
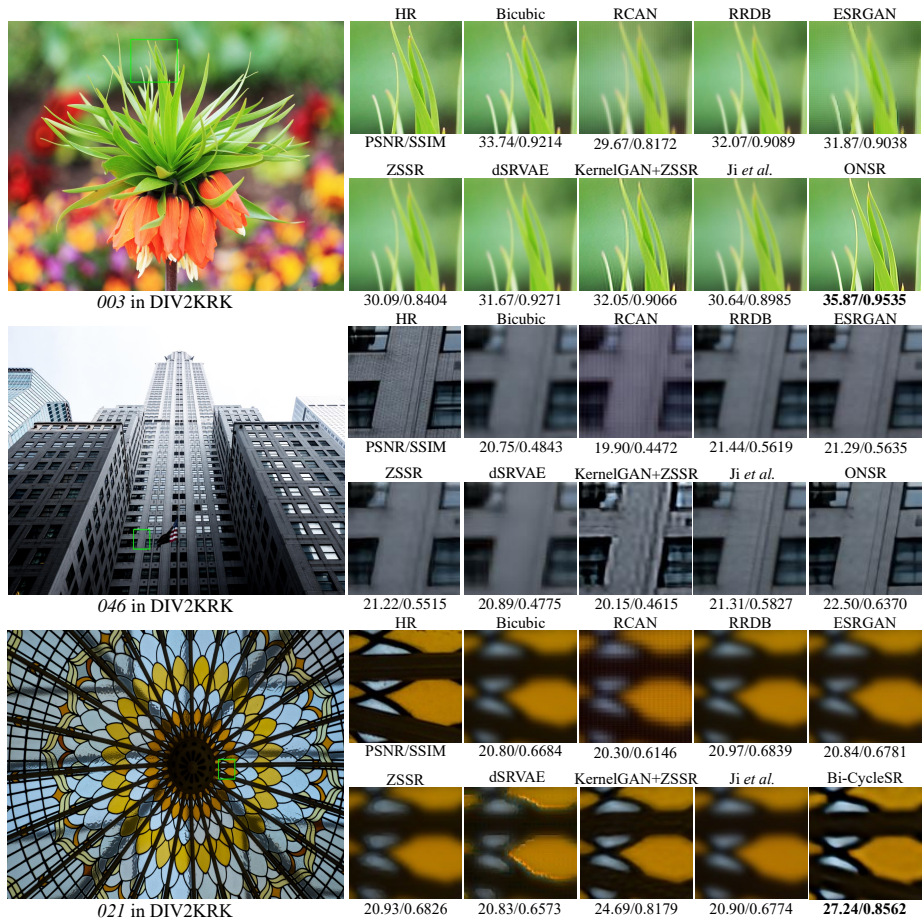
HR Bicubic RCAN RRDB ESRGAN

PSNR/SSIM 33.74/0.9214 29.67/0.8172 32.07/0.9089 31.87/0.9038

ZSSR dSRVAE KernelGAN+ZSSR Ji *et al.* ONSR

003 in DIV2KRK 30.09/0.8404 31.67/0.9271 32.05/0.9066 30.64/0.8985 **35.87/0.9535**

HR Bicubic RCAN RRDB ESRGAN

PSNR/SSIM 20.75/0.4843 19.90/0.4472 21.44/0.5619 21.29/0.5635

ZSSR dSRVAE KernelGAN+ZSSR Ji *et al.* ONSR

046 in DIV2KRK 21.22/0.5515 20.89/0.4775 20.15/0.4615 21.31/0.5827 22.50/0.6370

HR Bicubic RCAN RRDB ESRGAN

PSNR/SSIM 20.80/0.6684 20.30/0.6146 20.97/0.6839 20.84/0.6781

ZSSR dSRVAE KernelGAN+ZSSR Ji *et al.* Bi-CycleSR

021 in DIV2KRK 20.93/0.6826 20.83/0.6573 24.69/0.8179 20.90/0.6774 **27.24/0.8562**

Figure 6: Visual comparison of ONSR and SotA SR methods for $4\times$ SR. The model name is denoted above the corresponding patch and PSNR/SSIM is denoted below.

4. Experiments

4.1. Experimental Setup

Datasets. We use 800 HR images from the training set of DIV2K [30] as the external HR dataset and evaluate the SR performance on *DIV2KRK* [14]. LR images in DIV2KRK are generated by blurring and subsampling each image from the validation set (100 images) of DIV2K with randomly generated kernels. These kernels are isotropic or anisotropic Gaussian kernels with random lengths $\lambda_1, \lambda_2 \sim \mathcal{U}(0.6, 5)$ independently distributed for each axis, rotated by a random angle $\theta \sim \mathcal{U}[-\pi, \pi]$. To

Table 2: Quantitative comparison on DIV2KRK dataset. ×2 and ×4 denote the scale factors. ↑ denotes the larger the better. ↓ denotes the smaller the better. Best and second best results are **highlighted** and <u>underlined</u>.

Type	Method	×2				×4			
		PSNR ↑	SSIM ↑	PI ↓	LPIPS ↓	PSNR ↑	SSIM ↑	PI ↓	LPIPS ↓
Type 1: Non-BlindSR	Bicubic	28.81	0.8090	6.7039	0.3609	25.46	0.6837	8.6414	0.5572
	ZSSR [9]	29.09	0.8215	6.2707	0.3252	25.61	0.6920	8.1941	0.5192
	ESRGAN [3]	29.18	0.8212	6.1826	0.3178	25.57	0.6906	8.3554	0.5266
	RRDB [3]	29.19	0.8224	6.4801	0.3376	25.66	0.6937	8.5510	0.5416
	RCAN [2]	27.94	0.7885	6.8855	0.3417	24.75	0.6337	8.4560	0.5830
Type 2: BlindSR	Cornillere *et al.* [12]	29.42	0.8459	4.8343	**0.1957**	-	-	-	-
	dSRVAE [13]	-	-	-	-	25.07	0.6553	**5.7329**	0.4664
	Ji *et al.* [11]	-	-	-	-	25.41	0.6890	8.2348	0.5219
	KernelGAN+ZSSR [14]	<u>29.93</u>	<u>0.8548</u>	<u>5.2483</u>	0.2430	<u>26.76</u>	<u>0.7302</u>	7.2357	<u>0.4449</u>
	ONSR (Ours)	**31.34**	**0.8866**	**4.7952**	<u>0.2207</u>	**27.66**	**0.7620**	<u>7.2298</u>	**0.4071**

deviate from a regular Gaussian kernel, uniform multiplicative noise (up to 25% of each pixel value of the kernel) is further applied.

Evaluation Metrics. To quantitatively compare the SR performance different methods, we use PSNR, SSIM [31], Perceptual Index (PI) [32] and Learned Perceptual Image Patch Similarity(LPIPS) [33]. Contrary to PSNR and SSIM, lower PI and LPIPS indicate higher perceptual quality.

Training Details. We randomly sample 10 patches of 32×32 from the LR image and 10 patches of $32s \times 32s$ from different HR images for each input minibatch, where s denotes the scaling factor. ADAM [34] optimizer with $\beta_1 = 0.9, \beta_2 = 0.999$ is used for optimization. We set the online updating step to 500 for each image, and the LR image is tested every 10 steps. To accelerate the optimization, we initialize ONSR with the bicubically pretrained model of RRDB, which is publicly available.

4.2. Super-Resolution on Synthetic Data

We compare ONSR with other state-of-the-art (SotA) methods on the synthetic dataset DIV2KRK. We present two types of algorithms for analysis: 1) *Type*1 includes ESRGAN [3], RRDB [3], RCAN [2] and ZSSR [9]. They are non-blind SotA SR methods trained on bicubically downsampled images. 2) *Type* 2 are blind SR methods

including KernelGAN+ZSSR [14], dSRVAE [13], Ji *et al*. [11] and Cornillere *et al*. [12].

Quantitative Results. SotA non-bind SR methods such as ESRGAN and RRDB have remarkable performance on bicubically downscaled images. However, as shown in Table 2 *Type* 1, when tested on DIV2KRK, they perform only slightly better than the naive bicubic interpolation. And RCAN is even worse. The performance drop suggests that these methods fail to generalize to the test images with various degradations in DIV2KRK. As a comparison, our ONSR outperforms these non-blind SR methods by a large margin. Specifically, RRDB shares the same network architectures with G_r in ONSR, while ONSR outperforms it by **2.15 dB** and **2 dB** for scales $\times 2$ and $\times 4$ respectively. This comparison demonstrates the effectiveness of the online updating strategy adopted by ONSR.

As shown in Table 2 *Type* 2, ONSR also shows its superiority over other blind SR methods. KernelGAN+ZSSR is a blind SR method that also adopts an online updating strategy. However, as we have discussed in Sec 3.1, it does not exploit information from the external dataset, which may restrict its performance. As a result, ONSR outperforms it by **1.41 dB** and **0.90 dB** for scales $\times 2$ and $\times 4$ respectively. This comparison indicates that ONSR successfully integrates information from both internal and external branches and achieves better SR performance.

Qualitative Results. In Figure 5 and 6, we present visual comparisons between these methods on scales $\times 2$ and $\times 4$ respectively. As shown in these figures, the images produced by SotA non-blind SR methods are not sharp enough. RCAN even changes the colors of the original images. The results produced by blind SR methods are relatively sharper, but they also tend to contain undesirable artifacts and distortions, such as the window contours in image *046*. As a comparison, the SR images produced by ONSR are cleaner and more visually favorable.
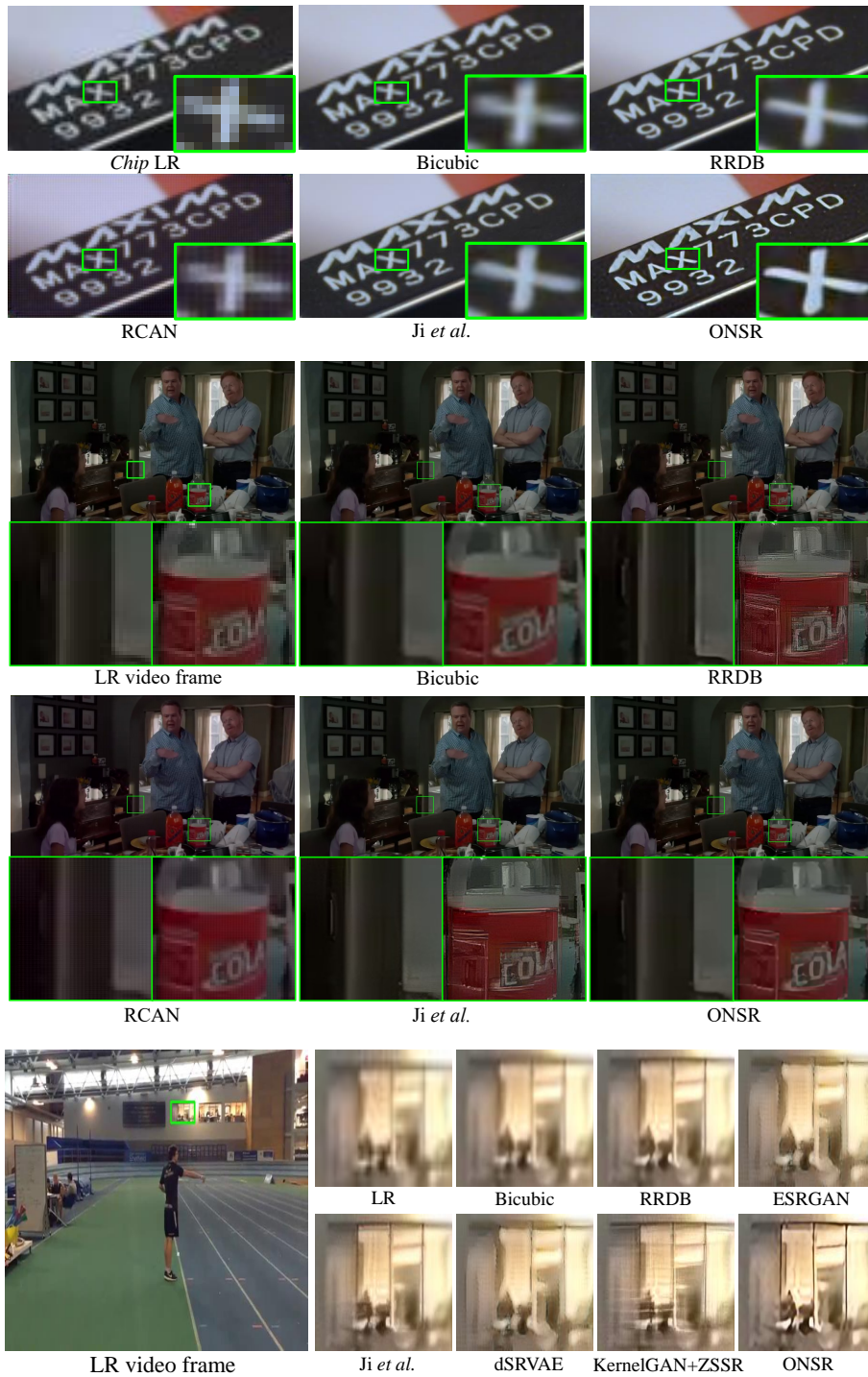
Figure 7: Visual comparison of model adaptation to the real image "*Chip*" and real-world video frames (from YouTube) for $4\times$ SR.

4.3. Super-Resolution on Real-World Data

To further demonstrate the effectiveness of ONSR in real scenarios, we conduct experiments on real images, which are more challenging due to the complicated and unknown degradations. Since there are no ground-truth HR images for calculating quantitative metrics, we only provide visual comparisons. As shown in Figure 7, the letter "X" in the real image "*Chip*" restored by RRDB, RCAN, Ji *et al.* and ZSSR are blurry or have unpleasant artifacts. As a comparison, the super-resolved image of ONSR has more shaper edges and is more visually pleasing. We also apply these methods to video frames from YouTube [1]. As shown in Figure 7, the generated $4\times$ SR frames from most methods are seriously blurred or contain numerous mosaics. While ONSR can produce visually promising images with clearer edges and fewer artifacts. This comparison further demonstrates the robustness of ONSR against various degradations in real scenarios.

Table 3: Quantitative comparison between ONSR with other SotA blind SR methods. The G_r in ONSR is initialized with RRDB-G, in which case our method is denoted as ONSR-G. Results on DIV2KRK are reported. Best and second best results are **highlighted** and <u>underlined</u>

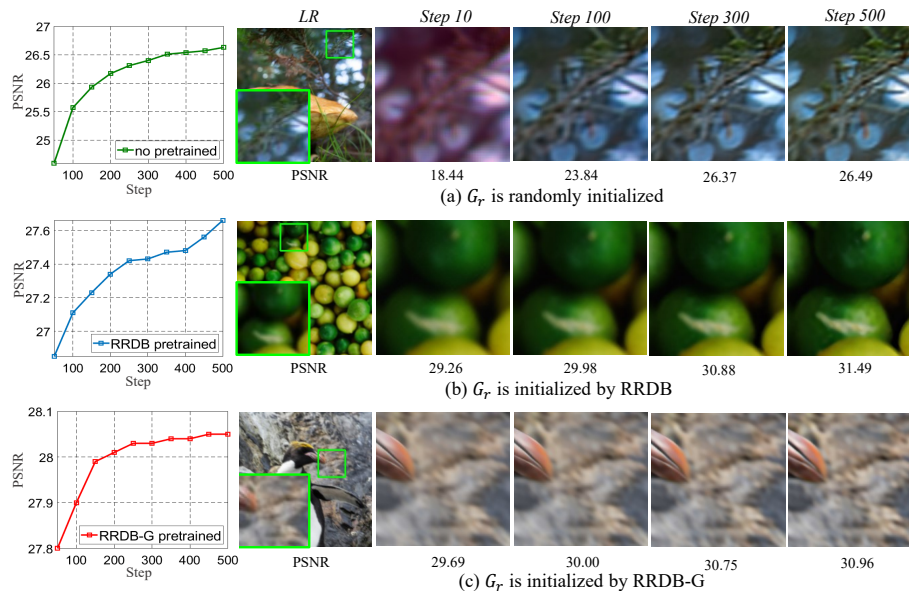| Method	Scale	PSNR ↑	SSIM ↑	PI↓	LPIPS↓
IKC [5]		<u>31.20</u>	<u>0.8767</u>	5.1511	0.2350
DASR [6]		30.72	0.8606	5.3947	0.2501
RRDB-G [3]	$\times 2$	31.18	0.8763	<u>4.8995</u>	<u>0.2213</u>
ONSR-G (Ours)		**31.69**	**0.8907**	**4.6036**	**0.1947**
KernelGAN [14] + USRNet [1]		24.32	0.6617	8.4425	0.5413
IKC [5]		27.69	0.7657	6.9027	0.3863
DASR [6]	$\times 4$	27.48	0.7549	7.2024	0.4027
RRDB-G [3]		<u>27.73</u>	<u>0.7660</u>	<u>6.8767</u>	<u>0.3834</u>
ONSR-G (Ours)		**28.05**	**0.7775**	**6.7716**	**0.3781**

---

[1] https://www.youtube.com

Figure 8: PSNR and visual results of ONSR with G_r is initialized (a) randomly, (b) by model trained on data synthesized by bicubic downsampling, and (c) by model trained on data synthesized by multiple Gaussian kernels.

4.4. Ablation Study

4.4.1. Study on the initialization of G_r

As we have discussed above, the SR module G_r in our ONSR is usually initialized with pretrained model weights to reduce the updating steps. In this section, we experimentally investigate the influence of different initialization methods. Two initialization methods are firstly considered: a) random initialization, and b) model pretrained on data synthesized by bicubic downsampling. As shown in Figure 8 (a) and (b), ONSR can converge well under both initialization, which demonstrates the good convergence of ONSR. In the meanwhile, carefully initialized G_r (case (b)) helps ONSR converge faster and has a better optimum point. It indicates that more powerful initialized G_r may further improve the performance of ONSR.

Recently, some methods (such as IKC [5] and DASR [6]) are proposed to train the SR model with data synthesized by multiple Gaussian kernels to improve its robustness. This strategy has proved to be effective in training an accurate model for
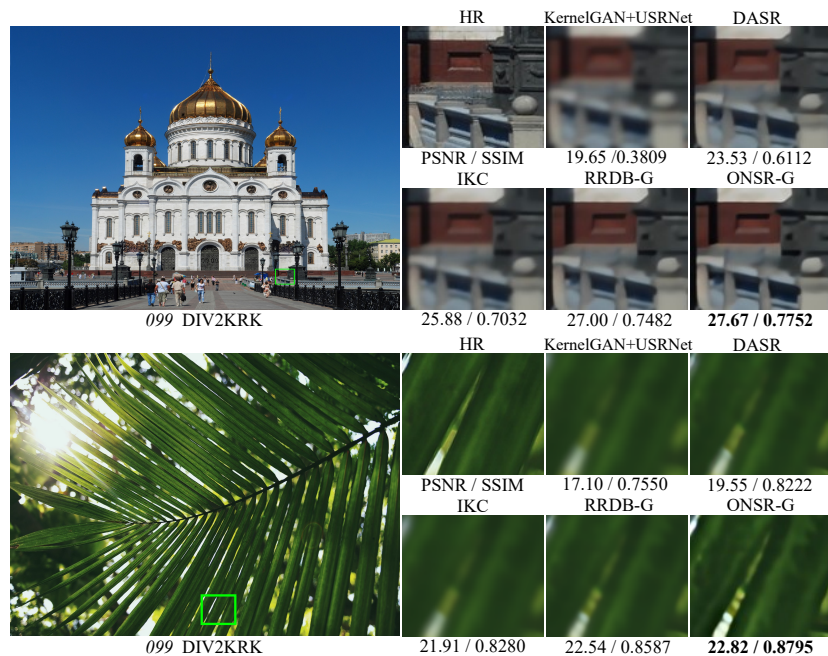
Figure 9: Visual comparison of ONSR-G and other methods for ×4 SR (image *026* and image *099*).

blind SR [35]. To explore the performance of ONSR when G_r is initialized with such a powerful model, we also train an RRDB on data synthesized by multiple isotropic Gaussian kernels, which is denoted as RRDB-G. We initialize G_r with RRDB-G, in which case our method is denoted as ONSR-G. As shown in Figure 8 (c), ONSR-G can still further improve the performance of the initialization model from 27.80 dB to a better point of 28.05 dB. As shown in Table 3, ONSR-G outperforms IKC by about **+0.4** dB on PSNR and **+0.012** on SSIM for scale factors ×2 and ×4 respectively. The visual comparisons are shown in Figure 9. As one can see, the results produced by ONSR-G are clearer and more visually favorable. This comparison indicates that our method can easily enjoy the merits of other powerful SR methods by taking them as the initialization models.

4.4.2. Study on the architecture of G_r

In the experiments above, we only use RRDB as G_r in our ONSR. In this subsection, we experimentally prove that the proposed method works well for G_r of different

20

Table 4: The performance of ONSR with G_r of different architectures. ON-$Arch$ denotes ONSR with the G_r of architecture named $Arch$. Results are reported on DIV2KRK with scale factor $\times 4$.

Method	PSNR↑	SSIM↑	PI↓	LPIPS↓
RDN [16]	25.66	0.6935	8.5341	0.5411
ON-RDN	**27.30**	**0.7498**	**7.4274**	**0.4377**
RCAN [2]	24.75	0.6337	8.4560	0.5830
ON-RCAN	**27.58**	**0.7612**	**7.1290**	**0.4020**

architectures. Specifically, we perform experiments on G_r of two other architectures, *i.e.* RDN [16] and RCAN [2]. As shown in Table 4, the original RDN and RCAN do not perform well on DIV2KRK. This is because their original models are trained on data synthesized by bicubic downsampling and can not well generalize to test images in DIV2KRK. As a comparison, Our online updating strategy can largely improve the performance of both models (denoted as ON-RDN and ON-RCAN respectively). For example, as shown in 4, the online updating strategy improves the PSNR results of RDN and RCAN by $+\mathbf{1.64}$ dB and $+\mathbf{2.73}$ dB respectively. It indicates that the online updating strategy of ONSR works well for G_r of different architectures.

4.4.3. Study on different modules in ONSR

To explain the roles of different modules (*i.e.* IB, EB and D_l) played in ONSR, we study four different variants of ONSR, which are denoted as *IBSR*, *EBSR*, *IB-EBSR*, and *IB-EB-GSR*. The details of these variants are shown in Figure 10 and explained
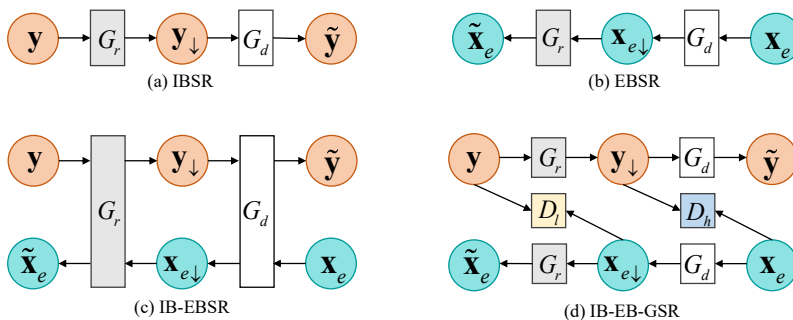

Figure 10: Details of different variants of ONSR.

below:

IBSR. IBSR only has an internal branch to exploit the internal properties of the test LR image for degradation estimation and SR reconstruction, which is optimized online.

EBSR. Contrary to IBSR, EBSR only has an external branch to capture general priors of external HR images, which is optimized offline. After offline training, we use the fixed module G_r to test LR images.

IB-EBSR. IB-EBSR has both internal branch and external branch but no GAN modules.

IB-EB-GSR. IB-EB-GSR has both D_l and D_h to explore the underlying distribution characteristics of the test LR and external HR images.

Table 5: Comparison of different variants of ONSR. Results are reported on DIV2KRK.

Method	Scale	PSNR	SSIM	Scale	PSNR	SSIM
IBSR		28.05	0.8277		25.51	0.6976
EBSR		30.82	0.8806		26.56	0.7249
IB-EBSR	$\times 2$	31.10	0.8850	$\times 4$	27.60	0.7609
IB-EB-GSR		31.29	0.8859		27.34	0.7507
ONSR		**31.34**	**0.8866**		**27.66**	**0.7620**

The quantitative comparisons on DIV2KRK are shown in Table 5. As one can see, IB-EBSR outperforms both IBSR and EBSR by a large margin. It indicates that both IB and EB are important for SR performance. The performance of IB-EBSR could be further improved if D_l is introduced. It suggests that adversarial training can help G_r to be better optimized. However, when D_l and D_h are both added in IB-EB-GSR, the performance is inferior to ONSR. In IB-EB-GSR, the initial SR results of $G_r(\mathbf{y})$ are likely to have unpleasant artifacts or distortions. Besides, the external HR image $\mathbf{x}_e$ can not provide directly pixelwise supervision to $G_r(\mathbf{y})$. Therefore, the application of D_h may affect the optimization of IB-EB-GSR and make it inferior to ONSR.

4.4.4. Study on separate optimization

As we have mentioned in Sec 3.4, we adopt separate optimization instead of the typically used joint optimization in our ONSR. In this section, we experimentally compare the two optimization strategies. In separate optimization, G_d and G_r are alternately optimized via the test LR image and external HR images respectively. While in joint optimization, both modules are optimized together. As shown in Table 6, separate optimization surpasses the joint optimization in all metrics for scale factors $\times 2$ and $\times 4$. We also compare the convergence of these two optimization strategies. We plot the PSNR and SSIM results of the two strategies every 100 steps. As shown in Figure 11, the results of separate optimization are not only higher but also grow faster than that of joint optimization. It suggests that separate optimization could not only help the network converge faster, but also help it converge to a better optimum point. It may be because that separate optimization divides the original highly complex problem into two simpler subproblems, and both of them are easier to be solved. Thus separate optimization could converge faster and reach a better optimum point. This property of separate optimization allows us to make a trade-off between SR effectiveness and efficiency by setting different training iterations.

Table 6: Comparisons between separate optimization and joint optimization. Results are reported on DIV2KRK.

Method	Scale	PSNR↑	SSIM↑	PI↓	LPIPS↓
Joint Optimization	$\times 2$	31.03	0.8827	4.8759	0.2212
Separate Optimization		**31.34**	**0.8860**	**4.7952**	**0.2207**
Joint Optimization	$\times 4$	26.97	0.7399	7.5985	0.4445
Separate Optimization		**27.66**	**0.7620**	**7.2298**	**0.4071**

4.4.5. Study on the External data

In this section, we perform experiments to study the influence of the external HR data. Firstly, we investigate how the number of external HR images will influence SR performance. we randomly sample 200, 400, 600, 700, and all 800 HR images from the training set of DIV2K as the external data and perform $4\times$ SR on DIV2KRK. As
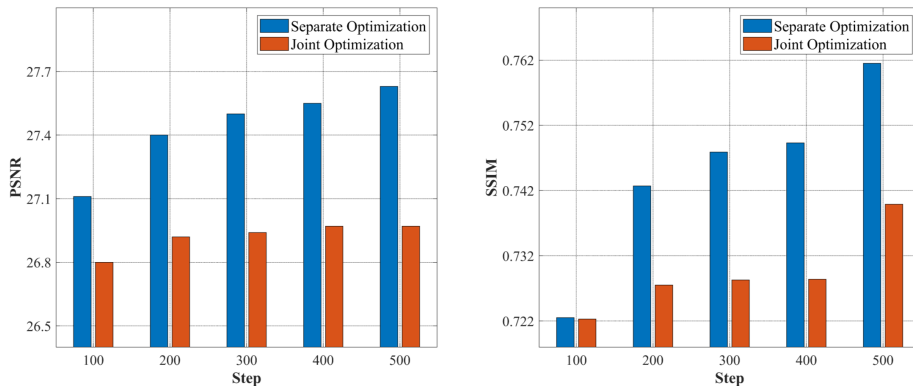
Figure 11: The average PSNR (left) and SSIM (right) of *Joint Optimization* and *Separate Optimization* for $4\times$ SR in differente training steps.

shown in Table 7, the performance of ONSR is continuously improved as the number of HR images increases. It indicates that more external HR images could help ONSR learn better general priors. Secondly, we investigate the influence of different external HR datasets. We use another popular dataset Flickr2K that consists of 2650 HR images as the external dataset. As can be seen from Table 7, the SR performance achieved with DIV2K is comparable to that with Flickr2K. Therefore, the SR performance tends to be stable when the number of external HR images is large enough, and 800 HR images from DIV2K could be sufficient for one test LR image.

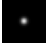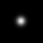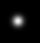Table 7: Performance of ONSR when different number of external HR images are used. Results are reported on DIV2KRK.
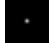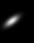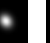
# External HR	200	400	600	700	800 (DIV2K)	2650 (Flickr2K)
PSNR	26.93	26.97	27.58	27.60	27.66	27.65
SSIM	0.7390	0.7399	0.7606	0.7610	0.7620	0.7629

4.5. Non-Blind Setting

In this subsection, we explore the upper boundary of ONSR in a non-blind setting. We replace G_d in ONSR with the ground-truth blur kernel (denoted as ONSR-NonBlind). Following the setting in [1], we evaluate our methods on *BSD68* [36], and 12 representative and diverse blur kernels are used to synthesize test LR images,

including 4 isotropic Gaussian kernels with different widths, 4 anisotropic Gaussian kernels from [10], and 4 motion blur kernels from [37, 38]. The quantitative results are shown in Table 8. As one can see, under the non-blind setting, ONSR achieves the best performance among the reference methods. We need to note that USRNet [1] is a SotA non-blind method, while ONSR still outperforms it by a large margin on all 12 kernels. For example, under the first blur kernel, ONSR outperforms USRNet by $+\mathbf{1.11}$ dB and $+\mathbf{1.21}$ dB for scale factors $\times 2$ and $\times 4$ respectively. It demonstrates that the online updating strategy of ONSR also works well in a non-blind setting.

Table 8: Average PSNR results of non-blind setting for $4\times$ SR. Best and second best results are **highlighted** and <u>underlined</u>.

Method	Scale												
EDSR [39]		25.54	27.82	20.59	21.34	27.66	27.28	26.90	26.07	27.14	26.96	19.72	19.86
RCAN [2]		29.48	26.76	25.31	24.37	24.38	24.10	24.25	23.63	20.31	20.45	20.57	22.04
ZSSR [9]	$\times 2$	29.44	29.48	28.57	27.42	27.15	26.81	27.09	26.25	14.22	14.22	16.02	19.39
IRCNN [40]		29.60	30.16	29.50	28.37	28.07	27.95	28.21	27.19	28.58	26.79	29.02	28.96
USRNet [1]		<u>30.55</u>	<u>30.96</u>	<u>30.56</u>	<u>29.49</u>	<u>29.13</u>	<u>29.12</u>	<u>29.28</u>	<u>28.28</u>	<u>30.90</u>	<u>30.65</u>	<u>30.60</u>	<u>30.75</u>
ONSR-NonBlind		**31.66**	**31.98**	**31.40**	**30.17**	**29.76**	**29.63**	**29.86**	**28.87**	**30.93**	**30.78**	**30.80**	**31.12**
EDSR [39]		21.45	22.73	21.60	20.62	23.16	23.66	23.16	23.00	24.00	23.78	19.79	19.67
RCAN [2]		22.68	25.31	25.59	24.63	24.37	24.23	24.43	23.74	20.06	20.05	20.33	21.47
ZSSR [9]	$\times 4$	23.50	24.33	24.56	24.65	24.52	24.20	24.56	24.55	16.94	16.43	18.01	20.68
IRCNN [40]		23.99	25.01	25.32	25.45	25.36	25.26	25.34	25.47	24.69	24.39	24.44	24.57
USRNet [1]		<u>25.30</u>	<u>25.96</u>	<u>26.18</u>	<u>26.29</u>	<u>26.20</u>	<u>26.15</u>	<u>26.17</u>	<u>26.30</u>	<u>25.91</u>	<u>25.57</u>	<u>25.76</u>	<u>25.70</u>
ONSR-NonBlind		**26.51**	**27.24**	**27.50**	**27.57**	**27.43**	**27.30**	**27.36**	**27.51**	**26.17**	**26.17**	**26.21**	**26.30**

4.6. Speed Comparison

We test the speed of different blind SR methods to compare their overall performance in terms of effectiveness and efficiency. We evaluate their average running time on DIV2KRK for $\times 2$ on the same machine with an NVIDIA 2080Ti GPU. Since IKC [5] and DASR [6] are included in the referring methods, we report the performance of ONSR-G for fair comparisons. We need to note that the running time of ONSR-G is closely related to its online updating steps. In previous experiments, the steps are set as 500 for best performance. However, as we have discussed in Sec 4.4.4, due to the good convergence of ONSR-G, we can set fewer steps to make a balance between accuracy and speed. Thus, we also test the performance of ONSR-G when steps are 5, 10, and

100 for comparisons. We use ONSR-G-S to denote ONSR-G with updating steps as S. As shown in Table 9, ONSR-G-5 outperforms KernelGAN + ZSSR [14] and Cornillere *et al.* by $+\mathbf{4.39}$ dB and $+\mathbf{1.73}$ dB while with $\mathbf{174}$ times and 21 times faster speed respectively. When compared with IKC, ONSR-G-10 also achieves a similar PSNR result with a comparable speed. DASR is much faster than the other methods, but its PNSR result is suboptimal. On the whole, ONSR-G can achieve competing performance with the most recent blind SR methods. Moreover, the good convergence of ONSR allows us to easily adjust its running time according to different scenarios.

Table 9: Average inference time comparison on DIV2KRK for $\times 2$ SR. ONSR-G-S denotes ONSR-G with updating steps as S.

Method	Speed(s/image)	PSNR(dB)
KernelGAN + ZSSR [14]	1127.84	26.76
Cornillere *et al.* [12]	135.51	29.42
IKC [5]	7.14	31.20
DASR [6]	0.24	30.72
ONSR-G-5 (Ours)	6.47	31.15
ONSR-G-10 (Ours)	8.00	31.21
ONSR-G-100 (Ours)	75.29	31.61

5. Conclusion and Future Work

In this paper, we argue that most nowadays SR methods are not image-specific. Towards the limitation, we propose an online SR (ONSR) method, which could customize a specific model for each test image. In detail, we design two branches, namely internal branch (IB) and external branch (EB). IB could learn the specific degradation of the test image, and EB could learn to super resolve images that are degraded by the learned degradation. IB involves only the LR image, while EB uses external HR images. In this way, ONSR could leverage the benefits of both inherent information of the test LR image and general priors from external HR images. Extensive experiments on both synthetic and real-world images prove the superiority of ONSR in the blind SR problem. These results indicate that customizing a model for each test image is more practical in real applications than training a general model for all LR images.

26

Moreover, the speed of ONSR may be further improved by designing more lightweight modules for faster inference or elaborating the training strategy to accelerate convergence. Faster speed can help it to be more practical when processing large amounts of test images, such as videos of low resolution, which is also the focus of our future work.

References

[1] K. Zhang, L. V. Gool, R. Timofte, Deep unfolding network for image super-resolution, in: Proceedings of the IEEE/CVF Conference on Computer Vision and Pattern Recognition, 2020, pp. 3217–3226.

[2] Y. Zhang, K. Li, K. Li, L. Wang, B. Zhong, Y. Fu, Image super-resolution using very deep residual channel attention networks, in: Proceedings of the European Conference on Computer Vision, 2018, pp. 286–301.

[3] X. Wang, K. Yu, S. Wu, J. Gu, Y. Liu, C. Dong, Y. Qiao, C. Change Loy, Esrgan: Enhanced super-resolution generative adversarial networks, in: Proceedings of the European Conference on Computer Vision Workshops, 2018, pp. 0–0.

[4] Y. Yang, Y. Qi, Image super-resolution via channel attention and spatial graph convolutional network, Pattern Recognition 112 (2021) 107798.

[5] J. Gu, H. Lu, W. Zuo, C. Dong, Blind super-resolution with iterative kernel correction, in: Proceedings of the IEEE/CVF Conference on Computer Vision and Pattern Recognition, 2019, pp. 1604–1613.

[6] L. Wang, Y. Wang, X. Dong, Q. Xu, J. Yang, W. An, Y. Guo, Unsupervised degradation representation learning for blind super-resolution, in: Proceedings of the IEEE/CVF Conference on Computer Vision and Pattern Recognition, 2021, pp. 10581–10590.

[7] I. Goodfellow, J. Pouget-Abadie, M. Mirza, B. Xu, D. Warde-Farley, S. Ozair, A. Courville, Y. Bengio, Generative adversarial nets, Advances in neural information processing systems 27.

[8] C. Dong, C. C. Loy, K. He, X. Tang, Learning a deep convolutional network for image super-resolution, in: European Conference on Computer Vision, Springer, 2014, pp. 184–199.

[9] A. Shocher, N. Cohen, M. Irani, "zero-shot" super-resolution using deep internal learning, in: Proceedings of the IEEE/CVF Conference on Computer Vision and Pattern Recognition, 2018, pp. 3118–3126.

[10] K. Zhang, W. Zuo, L. Zhang, Learning a single convolutional super-resolution network for multiple degradations, in: Proceedings of the IEEE/CVF Conference on Computer Vision and Pattern Recognition, 2018, pp. 3262–3271.

[11] X. Ji, Y. Cao, Y. Tai, C. Wang, J. Li, F. Huang, Real-world super-resolution via kernel estimation and noise injection, in: Proceedings of the IEEE/CVF Conference on Computer Vision and Pattern Recognition Workshops, 2020, pp. 466–467.

[12] V. Cornillere, A. Djelouah, W. Yifan, O. Sorkine-Hornung, C. Schroers, Blind image super-resolution with spatially variant degradations, ACM Transactions on Graphics (TOG) 38 (6) (2019) 1–13.

[13] Z.-S. Liu, W.-C. Siu, L.-W. Wang, C.-T. Li, M.-P. Cani, Unsupervised real image super-resolution via generative variational autoencoder, in: Proceedings of the IEEE/CVF Conference on Computer Vision and Pattern Recognition Workshops, 2020, pp. 442–443.

[14] S. Bell-Kligler, A. Shocher, M. Irani, Blind super-resolution kernel estimation using an internal-gan, in: NeurIPS, 2019.

[15] N. Ahn, J. Yoo, K.-A. Sohn, Simusr: A simple but strong baseline for unsupervised image super-resolution, in: Proceedings of the IEEE/CVF Conference on Computer Vision and Pattern Recognition Workshops, 2020, pp. 474–475.

[16] Y. Zhang, Y. Tian, Y. Kong, B. Zhong, Y. Fu, Residual dense network for image super-resolution, in: Proceedings of the IEEE/CVF Conference on Computer Vision and Pattern Recognition, 2018, pp. 2472–2481.

[17] K. He, X. Zhang, S. Ren, J. Sun, Deep residual learning for image recognition, in: Proceedings of the IEEE/CVF Conference on Computer Vision and Pattern Recognition, 2016, pp. 770–778.

[18] G. Huang, Z. Liu, L. Van Der Maaten, K. Q. Weinberger, Densely connected convolutional networks, in: Proceedings of the IEEE conference on computer vision and pattern recognition, 2017, pp. 4700–4708.

[19] R. Chen, H. Zhang, J. Liu, Multi-attention augmented network for single image super-resolution, Pattern Recognition 122 (2022) 108349.

[20] Y. Wang, L. Wang, H. Wang, P. Li, H. Lu, Blind single image super-resolution with a mixture of deep networks, Pattern Recognition 102 (2020) 107169.

[21] Y. Liang, R. Timofte, J. Wang, S. Zhou, Y. Gong, N. Zheng, Single-image super-resolution-when model adaptation matters, Pattern Recognition (2021) 107931.

[22] T. Michaeli, M. Irani, Nonparametric blind super-resolution, in: Proceedings of the IEEE/CVF International Conference on Computer Vision, 2013, pp. 945–952.

[23] D. Ulyanov, A. Vedaldi, V. Lempitsky, Deep image prior, in: Proceedings of the IEEE/CVF Conference on Computer Vision and Pattern Recognition, 2018, pp. 9446–9454.

[24] D. Ren, K. Zhang, Q. Wang, Q. Hu, W. Zuo, Neural blind deconvolution using deep priors, in: Proceedings of the IEEE/CVF Conference on Computer Vision and Pattern Recognition, 2020, pp. 3341–3350.

[25] J. Pan, D. Sun, H. Pfister, M.-H. Yang, Blind image deblurring using dark channel prior, in: Proceedings of the IEEE/CVF Conference on Computer Vision and Pattern Recognition, 2016, pp. 1628–1636.

[26] J. Pan, Z. Hu, Z. Su, M.-H. Yang, Deblurring text images via l0-regularized intensity and gradient prior, in: Proceedings of the IEEE/CVF Conference on Computer Vision and Pattern Recognition, 2014, pp. 2901–2908.

[27] T. Michaeli, M. Irani, Blind deblurring using internal patch recurrence, in: European Conference on Computer Vision, Springer, 2014, pp. 783–798.

[28] S. Arora, N. Cohen, E. Hazan, On the optimization of deep networks: Implicit acceleration by overparameterization, in: International Conference on Machine Learning, PMLR, 2018, pp. 244–253.

[29] K. Simonyan, A. Zisserman, Very deep convolutional networks for large-scale image recognition, CoRR abs/1409.1556.

[30] E. Agustsson, R. Timofte, Ntire 2017 challenge on single image super-resolution: Dataset and study, in: Proceedings of the IEEE/CVF Conference on Computer Vision and Pattern Recognition Workshops, 2017, pp. 126–135.

[31] Z. Wang, A. C. Bovik, H. R. Sheikh, E. P. Simoncelli, Image quality assessment: from error visibility to structural similarity, IEEE transactions on image processing 13 (4) (2004) 600–612.

[32] Y. Blau, R. Mechrez, R. Timofte, T. Michaeli, L. Zelnik-Manor, The 2018 pirm challenge on perceptual image super-resolution, in: Proceedings of the European Conference on Computer Vision Workshops, 2018, pp. 0–0.

[33] R. Zhang, P. Isola, A. A. Efros, E. Shechtman, O. Wang, The unreasonable effectiveness of deep features as a perceptual metric, in: Proceedings of the IEEE/CVF Conference on Computer Vision and Pattern Recognition, 2018, pp. 586–595.

[34] D. P. Kingma, J. Ba, Adam: A method for stochastic optimization, arXiv preprint arXiv:1412.6980.

[35] L. Xie, X. Wang, C. Dong, Z. Qi, Y. Shan, Finding discriminative filters for specific degradations in blind super-resolution, Advances in Neural Information Processing Systems 34.

[36] D. Martin, C. Fowlkes, D. Tal, J. Malik, A database of human segmented natural images and its application to evaluating segmentation algorithms and measuring

ecological statistics, in: Proceedings of the IEEE/CVF International Conference on Computer Vision, IEEE, 2001.

[37] G. Boracchi, A. Foi, Modeling the performance of image restoration from motion blur, IEEE Transactions on Image Processing 21 (8) (2012) 3502–3517.

[38] A. Levin, Y. Weiss, F. Durand, W. T. Freeman, Understanding and evaluating blind deconvolution algorithms, in: Proceedings of the IEEE/CVF Conference on Computer Vision and Pattern Recognition, IEEE, 2009, pp. 1964–1971.

[39] B. Lim, S. Son, H. Kim, S. Nah, K. Mu Lee, Enhanced deep residual networks for single image super-resolution, in: Proceedings of the IEEE/CVF Conference on Computer Vision and Pattern Recognition Workshops, 2017, pp. 136–144.

[40] K. Zhang, W. Zuo, S. Gu, L. Zhang, Learning deep cnn denoiser prior for image restoration, in: Proceedings of the IEEE/CVF Conference on Computer Vision and Pattern Recognition, 2017, pp. 3929–3938.